Pure Appl. Geophys. 175 (2018), 2609–2622
© 2018 Springer International Publishing AG, part of Springer Nature
https://doi.org/10.1007/s00024-018-1828-7

Pure and Applied Geophysics

Estimating Q Factor from Multi-mode Shallow-Seismic Surface Waves

Lingli Gao,[1] Yudi Pan,[2] Gang Tian,[1] and Jianghai Xia[1]

Abstract—Surface waves are widely used in delineating subsurface structures. Surface-wave phase information (phase velocity) can be used for estimating near-surface S-wave velocity, and its amplitude information (attenuation coefficient) is used for characterizing near-surface quality (Q) factor. Multi-modal phenomenon of surface waves is commonly seen in shallow seismic, however, the existence of higher modes will introduce errors in the calculated surface-wave attenuation coefficients, which further reduces the accuracy of estimated Q factors. We propose to separate surface waves of different modes, and calculate surface-wave attenuation coefficients using single mode. Two synthetic cases are presented to show that errors would be introduced in the attenuation coefficients when multi-mode surface waves and body waves exist, and can be excluded if different modes of surface waves and body waves are separated beforehand. A real-world case demonstrates the feasibility of inverting surface-wave attenuation coefficients for the estimation of Q factor with our proposed method.

Key words: Surface wave, mode separation, Q factor.

1. Introduction

Quality (Q) factor and its inverse (dissipation factor, Q^{-1}) can be used to describe the attenuation of seismic wave. The Q factor, as a function of depth, is of fundamental interest in groundwater, geotechnical, environmental studies, geophysical exploration, and earthquake seismology. The propagation of surface waves is strongly influenced by the intrinsic dissipation of media. Modeling analysis (Xia et al. 2002, 2012) showed that shear-wave quality factor (Q_S) can be estimated by inverting Rayleigh wave attenuation coefficients. And compressional wave quality factor (Q_P) may be inverted when V_S/V_P is greater than 0.45 (Xia et al. 2002). Werning et al. (2013) estimated the distribution of the Q_S and Q_P from surface waves contained in land seismic data with this method. Ivanov et al. (2014) obtained quality factors of an Arctic ice-sheet site successfully from MASW data. Similar to the process of Rayleigh wave, Qs can be determined from high-frequency Love-wave data (Xia et al. 2013).

Surface waves are multi-modal in non-homogeneous media, and the multi-mode characteristic is widely observed in shallow seismic using multi-station approach (Foti et al. 2011). Investigation depth as well as accuracy of the inverted S-wave velocity can be significant improved by a joint inversion of multi-mode surface-wave dispersion curves (Xia et al. 2003; Maraschini and Foti 2010; Shen et al. 2016). However, the existence of multi-mode surface waves (including higher modes and leaky-wave mode; Gao et al. 2014, 2016) in the shallow surface-wave recordings will introduce errors in the attenuation coefficients, which will further reduce the accuracy of Q factor estimation (Misbah and Strobbia, 2014).

One important prerequisite for a successful application of Q factor estimation is to extract accurate attenuation coefficients. Therefore, we propose a new way to estimate attenuation coefficients from multi-mode surface waves. A new pre-processing step of separating surface waves of different modes is added prior to the calculation of attenuation coefficients. Then single-mode (fundamental-mode) surface wave is used for estimating attenuation coefficients. Due to the linear relationship between dissipation factor (Q^{-1}) and attenuation coefficients, we solve a damped least-square problem to determine Q factor from single-mode surface-wave attenuation coefficients. An L-curve method is used to find an

[1] School of Earth Sciences, Zhejiang University, 38 Zheda Rd, Hangzhou, Zhejiang, China.
[2] Geophysical Institute, Karlsruhe Institute of Technology (KIT), Hertzstr. 16, Karlsruhe, Germany. E-mail: yudi.pan@kit.edu; yudipan@yahoo.com

appropriate damping factor. Numerical examples are used to prove the significance of the proposed pre-processing step in estimating correct attenuation coefficient. A real-world data demonstrate the feasibility of estimating Q factor using the proposed method.

2. Attenuation Coefficients of Surface Waves

2.1. Calculation of Attenuation Coefficients

Phase information of high-frequency surface waves is directly related to the S-wave velocity of near-surface materials (Xia et al. 1999; Socco et al. 2010) and their amplitude information is related to attenuation coefficients (Xia et al. 2002, 2012, 2013). After performing Fourier transform to the raw dataset, we can obtain attenuation coefficients from surface-wave amplitude information. However, when using raw datasets directly, negative values of attenuation coefficients (detailed interpretations are in the following section) arise at some frequencies, representing that surface-wave amplitude increase, rather than decrease with offset at these frequencies. These negative attenuation coefficients are physically unreliable.

The spectra of surface-wave recordings at two arbitrary positions in a layered media can be written as (Foti et al. 2011)

$$R_1(x,f) = \sum_m S_m(f)\mathrm{e}^{-\alpha_m \cdot x} \cdot \mathrm{e}^{i(k-k_m(f))\cdot x}, \quad (1)$$

$$R_2(x+dx,f) = \sum_m S_m(f)\mathrm{e}^{-\alpha_m \cdot (x+dx)} \cdot \mathrm{e}^{i(k-k_m(f))\cdot (x+dx)}, \quad (2)$$

where S_m is the source function, x is the distance from the source to the first receiver, α_m and k_m are the attenuation coefficients and wavenumbers of m-th mode, respectively. dx is the interval between two receivers. R_1 and R_2 are the spreading-corrected traces, in which the geometrical spreading contribution is removed. Attenuation coefficients can be determined by Eqs. (1) and (2). However, the relative amplitude of each mode of the surface wave (absolute value of S_m) is a function of frequency depends on the source moment, source depth, and the vertical velocity distribution (Aki and Richards 1980, Chapter 7), and is hard to be solved theoretically. Hence, it is difficult to acquire attenuation coefficients from multi-mode surface waves with Eqs. (1) and (2) directly.

To obtain the attenuation coefficients, we simplify Eqs. (1) and (2) into single-mode version as

$$R_{10}(x,f) = S_0(f)\mathrm{e}^{-\alpha_0 \cdot x} \cdot \mathrm{e}^{i(k-k_0(f))\cdot x}, \quad (3)$$

$$R_{20}(x+dx,f) = S_0(f)\mathrm{e}^{-\alpha_0 \cdot (x+dx)} \cdot \mathrm{e}^{i(k-k_0(f))\cdot (x+dx)}, \quad (4)$$

where R_{10} and R_{20} represent the fundamental-mode surface-wave signals extracted from R_1 and R_2, respectively. Thus, a pre-processing of mode separation to the multi-mode raw data is needed.

After the pre-processing of mode separation, we can use the amplitude spectrum of the fundamental-mode surface waves (R_{10} and R_{20}) to determine attenuation coefficients via

$$\alpha_{S0}(f) = -\frac{In\left(\left|\frac{R_{20}(x+dx,f)}{R_{10}(x,f)}\right|\right)}{dx}. \quad (5)$$

Surface waves are multi-modal in non-homogeneous media, and higher modes are frequently recorded and sometimes dominant in shallow-seismic wave fields. The amplitude of surface-wave recording is the sum of the displacements of multiple modes. Attenuation coefficients are calculated between every two traces, while an averaged attenuation coefficient of all the two-trace results is regarded as the final one for the inversion.

2.2. Mode Separation

Different Rayleigh wave modes normally interfere with each other in the t–x (time–space) domain. Usually, modes can be separated efficiently using frequency–wavenumber analysis in the f–k (frequency–wavenumber) or f–v (frequency–velocity) domain. We use a high-resolution linear Radon transform (LRT; Luo et al. 2008, 2009a, b) as the mode separation algorithm. In this method, different modes of surface waves are recognized and separated in the f–v domain, and then only single-mode dispersive energy is transformed back into t–x domain

to reconstruct single-mode surface wave. Amplitude and phase can be effectively preserved by high-resolution linear inverse Radon transform (Luo et al. 2008, 2009a, b). This preservation provides a basis for mode separation and mode reconstruction.

The LRT can be written in the matrix form as

$$\mathbf{d} = \mathbf{L}\mathbf{m}, \tag{6}$$

and its adjoint transform as

$$\mathbf{m}_{\text{adj}} = \mathbf{L}^{\mathbf{T}}\mathbf{d}, \tag{7}$$

where $\mathbf{L} = e^{i2\pi fpx}$ is the forward LRT operator, p is the slowness, $\mathbf{d}$ and $\mathbf{m}$ represent the shot gather and Radon panel, respectively. $\mathbf{m}_{\text{adj}}$ denotes the low-resolution Radon panel using the transpose or adjoint operator $\mathbf{L}^{\mathbf{T}}$. High-resolution dispersion image is hard to be achieved from standard LRT because they suffer from the loss of resolution and aliasing will arise owing to the incomplete information.

The following equation is defined by taking the sparsity constraint into consideration for finding the model $\mathbf{m}$, which can minimize the number of model-space parameters (Luo et al. 2008)

$$\begin{aligned}&\left(\mathbf{W}_{\mathbf{m}}^{-\mathbf{T}}\mathbf{L}^{\mathbf{T}}\mathbf{W}_{\mathbf{d}}^{\mathbf{T}}\mathbf{W}_{\mathbf{d}}\mathbf{L}\mathbf{W}_{\mathbf{m}}^{-1} + \alpha\mathbf{I}\right)\mathbf{W}_{\mathbf{m}}\mathbf{m}\\ &\quad = \mathbf{W}_{\mathbf{m}}^{-\mathbf{T}}\mathbf{L}^{\mathbf{T}}\mathbf{W}_{\mathbf{d}}^{\mathbf{T}}\mathbf{W}_{\mathbf{d}}\mathbf{d},\end{aligned} \tag{8}$$

where $\mathbf{I}$ denotes the identity matrix, $\mathbf{W_d}$ is the matrix of data weights, $\mathbf{W_m}$ is the matrix of model weights that is extremely important in the design of high-resolution Radon operators, $\mathbf{W}_{\mathbf{m}}^{-\mathbf{T}}$ is the transpose matrix of $\mathbf{W}_{\mathbf{m}}^{-1}$, and α maintains the balance between data misfit and model constraints. Conjugate gradient (CG) algorithm is efficient for solving Eq. (8), and more details about the algorithm can be found in Luo et al. (2009a). Similar preprocessing can be done using forward and inverse f–k transform. Here we use high-resolution LRT due to its higher resolution in distinguishing surface waves of different modes.

3. Inversion System

The relationship between fundamental-mode surface-wave attenuation coefficients and Q factor in a layered model is modified from Anderson et al. (1965)

$$\alpha_{S0}(f) = \frac{\pi f}{c_{S0}^2} \times \left[\sum_{i=1}^{n} \mathrm{P}_i(f) Q_{\mathrm{P}_i}^{-1} + \sum_{i=1}^{n} \mathrm{S}_i(f) Q_{\mathrm{S}_i}^{-1}\right] \quad \text{for Rayleigh wave,} \tag{9}$$

$$\alpha_{S0}(f) = \frac{\pi f}{c_{S0}^2} \times \sum_{i=1}^{n} \mathrm{S}_i(f) Q_{\mathrm{S}_i}^{-1} \quad \text{for Love wave,} \tag{10}$$

where

$$\mathrm{P}_i(f) = V_{\mathrm{P}_i} \frac{\partial c_{S0}(f)}{\partial V_{\mathrm{P}_i}},$$

$$\mathrm{S}_i(f) = V_{\mathrm{S}_i} \frac{\partial c_{S0}(f)}{\partial V_{\mathrm{S}_i}},$$

$\alpha_{S0}(f)$ is the fundamental-mode surface (Rayleigh/Love) wave attenuation coefficients, and f is the frequency. Q_{P_i} and Q_{S_i} are the Q factors for P- and S-wave of the i-th layer, respectively; V_{P_i} and V_{S_i} are the P-wave and S-wave velocities of the i-th layer, respectively. $c_{S0}(f)$ is the fundamental-mode surface-wave phase velocities; and n is the total number of layers.

Equations (9) and (10) show a linear relationship between surface wave attenuation coefficients and the dissipation factors (Q_{P}^{-1} and Q_{S}^{-1}). The attenuation caused by the influence of P-wave should be taking into consideration when the $V_{\mathrm{S}}/V_{\mathrm{P}}$ ratio is higher than 0.45 (Xia et al. 2002). After obtaining S-wave velocities by inverting surface wave velocities, the Q factor can be inverted directly using Eqs. (9) and (10). The inversion problem can be described by the following system (Xia et al. 2003):

$$\mathbf{A}\vec{X} = \vec{B} \ (x_i > 0), \tag{11}$$

where $\vec{X}$ is a vector of inverse Q factor ($1/Q$), $\vec{B}$ is the attenuation coefficients (a data vector), and $\mathbf{A}$ is the data kernel matrix determined by Eqs. (9) and (10).

Using the damped least-square algorithm, we can obtain the solution via

$$\vec{X} = \left(\mathbf{A}^{\mathbf{T}}\mathbf{A} + \lambda\mathbf{I}\right)\mathbf{A}^{\mathbf{T}}\vec{B}, \tag{12}$$

where $\mathbf{T}$ represent the transpose operator. $\mathbf{I}$ is the unit matrix. λ is the damping factor. We use an L-curved

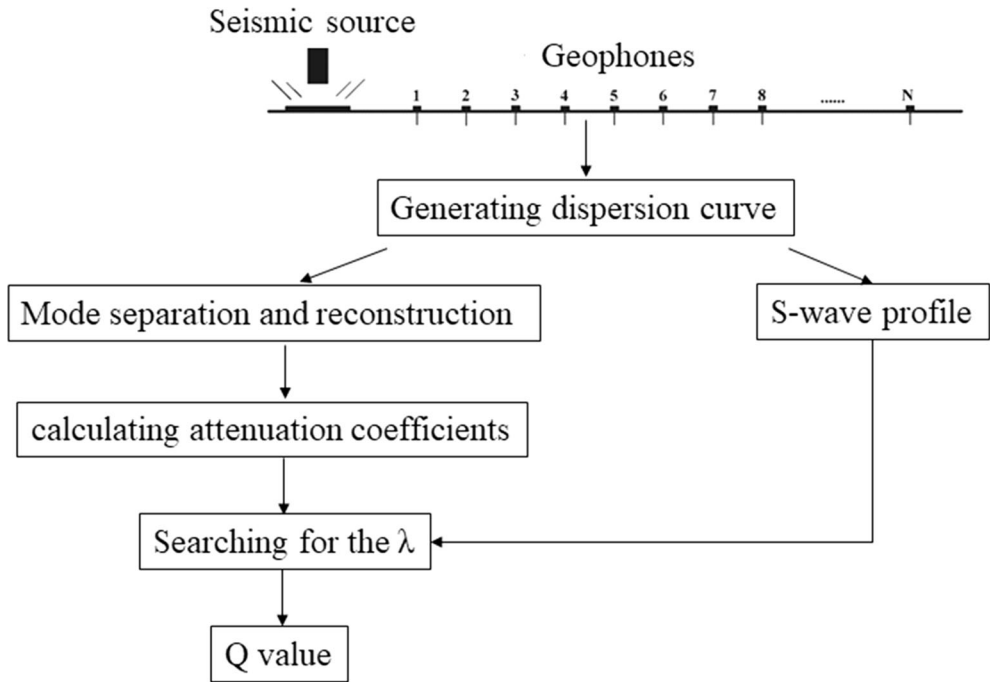

Figure 1
The flowchart of the process for estimating the Q value

Table 1

The parameters of a model containing a simple layer overlaying the half-space

Layer number	V_S (m/s)	V_P (m/s)	Density (g/cm^3)	h (m)	Q_S	Poisson's ratio
1	200	800	2	5	50	0.467
2	400	1500	2.1	∞	50	0.429

Q_P is set equal to Q_S

method (Lawson and Hanson 1974; Hansen 1992, 1998) to search for an appropriate damping factor λ. It seeks a regularized solution that is a trade-off between data (attenuation coefficients) misfit and model (Q factor) length. Herein, an L-value can be defined as

$$\mathbf{L}\left(\overrightarrow{X},\lambda\right) = \left\|\mathbf{S}\left(\mathbf{A}\overrightarrow{X} - \overrightarrow{B}\right)\right\|_2 + \lambda\left\|\overrightarrow{X}\right\|_\infty = \varphi_d + \lambda\varphi_m, \quad (13)$$

where $\boldsymbol{S}$ is related to a weight matrix $\mathbf{W} = \mathbf{S}^{\mathbf{T}}\mathbf{S}$ that is determined by errors in attenuation coefficients. The weighting matrix $\boldsymbol{W}$ is diagonal and positive. $\varphi_d = \left\|\mathbf{S}\left(\mathbf{A}\overrightarrow{X} - \overrightarrow{B}\right)\right\|_2$ is the data misfit, and $\varphi_m = \left\|\overrightarrow{X}\right\|_\infty$ is the model length, which is the maximum component of $\overrightarrow{X}$. A plot of (φ_m, φ_d) usually presents the shape of the L curve. Models corresponding to small damping factors usually possess large errors and result in long model lengths with small data misfits. While models corresponding to larger damping factors are usually stable, however, with relatively large data misfits and short model lengths. A trade-off model could be selected in the trade-off zone on the plot of (φ_m, φ_d). A detail flowchart (Fig. 1) is displayed to present the whole process.

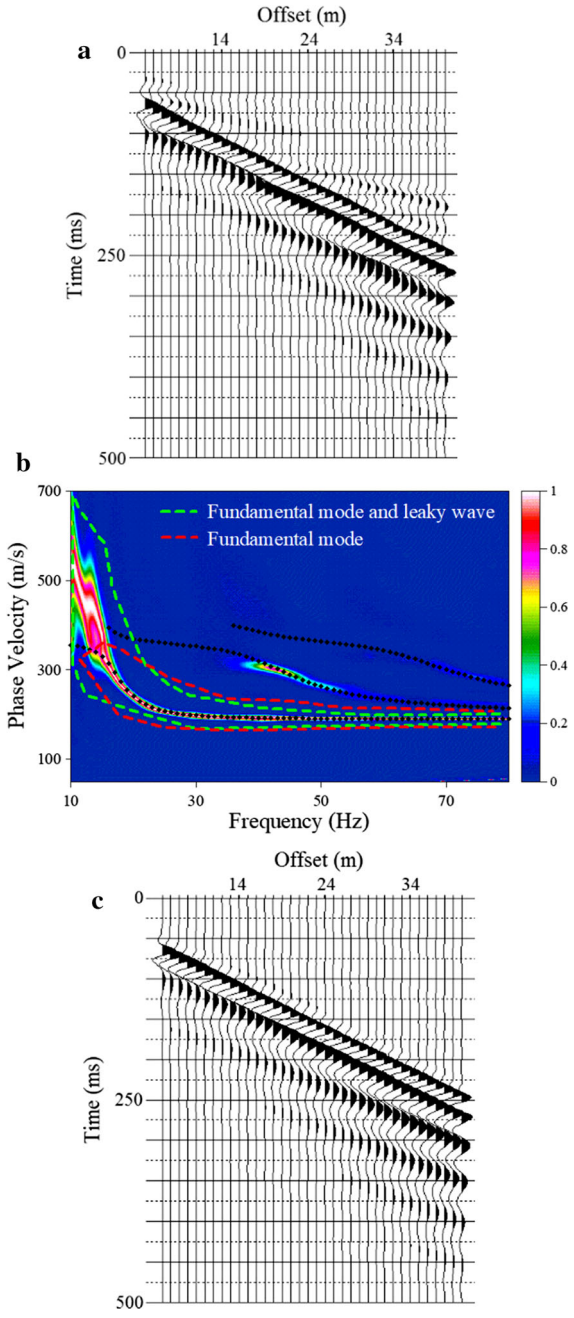

Figure 2

a Synthetic shot gather for the model shown in Table 1. **b** Dispersion image of the shot gather obtained by high resolution linear Radon transform. The dark dots are theoretical phase velocities. The green contour line contains both the fundamental- and leaky-mode energy, which is used as the second input dataset. The red contour line contains the fundamental-mode energy only, which is used as the third dataset. **c** Fundamental-mode shot gather obtained from the dispersive energy selected in the red dashed contour line in (**b**)

4. Synthetic Examples

We use two synthetic examples to verify our proposed method. The first example is a model containing a single surface layer overlying the half-space (Table 1). A 2D, viscoelastic-wave finite difference (FD) algorithm (Bohlen 2002) is used as a forward solver. The grid size and time step are chosen as 0.2 m and 0.05 ms to stabilize the FD modeling. The source wavelet is a 30 Hz Ricker wavelet with a 40 ms delay. An absorption mechanism based on generalized standard linear solid (GSLS) approach (Liu et al. 1976; Bohlen 2002) is used during the modeling to simulate the viscoelastic effect. 36 vertical component receivers are placed along the planner free surface, with a receiver interval of 1 m. The shot gather contains well-developed Rayleigh waves (Fig. 2a). High-resolution linear Radon transform is used to obtain the dispersion image (Fig. 2b). A dominant fundamental mode is visible. Higher modes are present, with relatively lower amplitude in the frequency range higher than 35 Hz. By plotting the theoretical dispersion curves (dark dots in Fig. 2b) on the top of the dispersion image, we can see that delineated dispersive energy below 15 Hz does not correspond to fundamental-mode surface waves. This part of dispersive energy is caused by a leaky surface wave (Gao et al. 2014), which appears when the Poisson's ratio is greater than 0.27. Fundamental- and leaky-mode energies are visually continuous in the low frequency range that we cannot distinguish.

We estimate the attenuation coefficients using three different datasets to prove the importance of performing mode separation in the preprocessing. The first dataset is the raw shot gather, and the attenuation coefficients (blue line in Fig. 3) estimated from the raw recording directly are much lower than theoretical attenuation coefficients calculated based on Eq. (9) (gray dashed line, Fig. 3), especially in the low (10–15 Hz) and middle (35–60 Hz) frequency ranges. The estimated attenuation coefficients include some negative values representing that surface-wave amplitude increase, rather than decrease with offset at these frequencies. These negative attenuation coefficients are physically unrealistic.

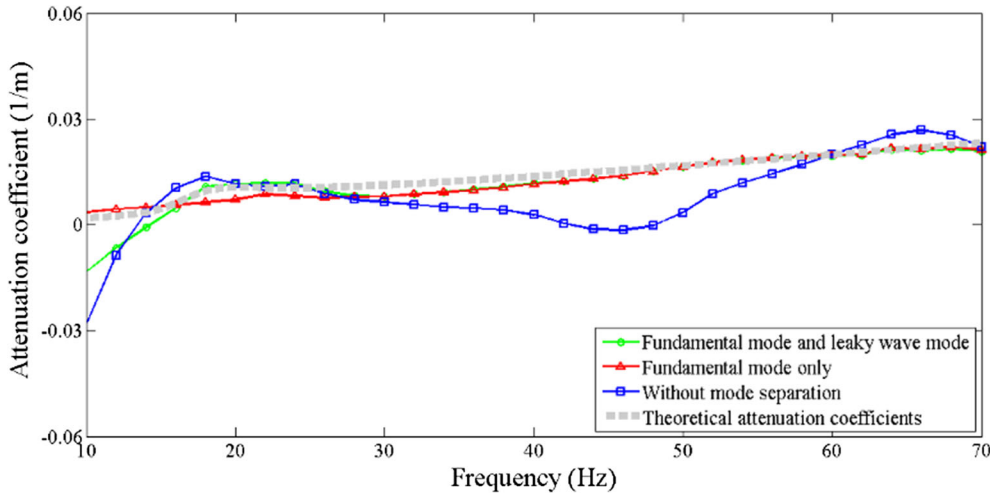

Figure 3
Comparison of attenuation coefficients obtained by different modes and theoretical attenuation coefficients

Table 2

The six-layer model with model parameters (Pan et al. 2013). Q_P is set equal to Q_S

Layer number	V_S (m/s)	V_P (m/s)	Density (g/cm^3)	h (m)	Q_S	Poisson's ratio
1	200	500	1.92	2	50	0.405
2	370	900	1.96	2	50	0.398
3	140	400	1.98	2	50	0.43
4	370	900	2	3	50	0.398
5	480	1200	2.02	4	50	0.405
6	600	1500	2.06	∞	50	0.405

The second dataset includes both fundamental- and leaky-mode surface waves. We manually select the dispersion energy of them and the rest are muted (green contour line in Fig. 2b) and transform them back into x–t domain to reconstruct a shot gather containing both fundamental- and leaky-mode surface waves. The attenuation coefficients (green line, Fig. 3) calculated from this dataset fit the theoretical values in the middle frequency range (35–60 Hz), indicating that the influences of higher mode are excluded. However, the attenuation coefficients are still negative in the low frequency range between 10 and 15 Hz, in which they have the same trend with those calculated from raw data. This is caused by the existence of leaky wave, which contaminate the estimated attenuation coefficients in the low frequencies.

The third dataset only includes fundamental-mode surface waves. We manually select fundamental-mode surface wave suggested by its theoretical phase velocities (black dots and red contour line in Fig. 2b), and reconstruct the correct fundamental-mode shot gather (Fig. 2c). Attenuation coefficients estimated from the fundamental mode (red lines in Fig. 3) nicely fit the theoretical attenuation coefficients (gray lines in Fig. 3). It indicates that both the existence of leaky-mode and high-mode surface waves will damage the accuracy of the attenuation coefficients in the frequency range they exist if they are not excluded from the shot gather.

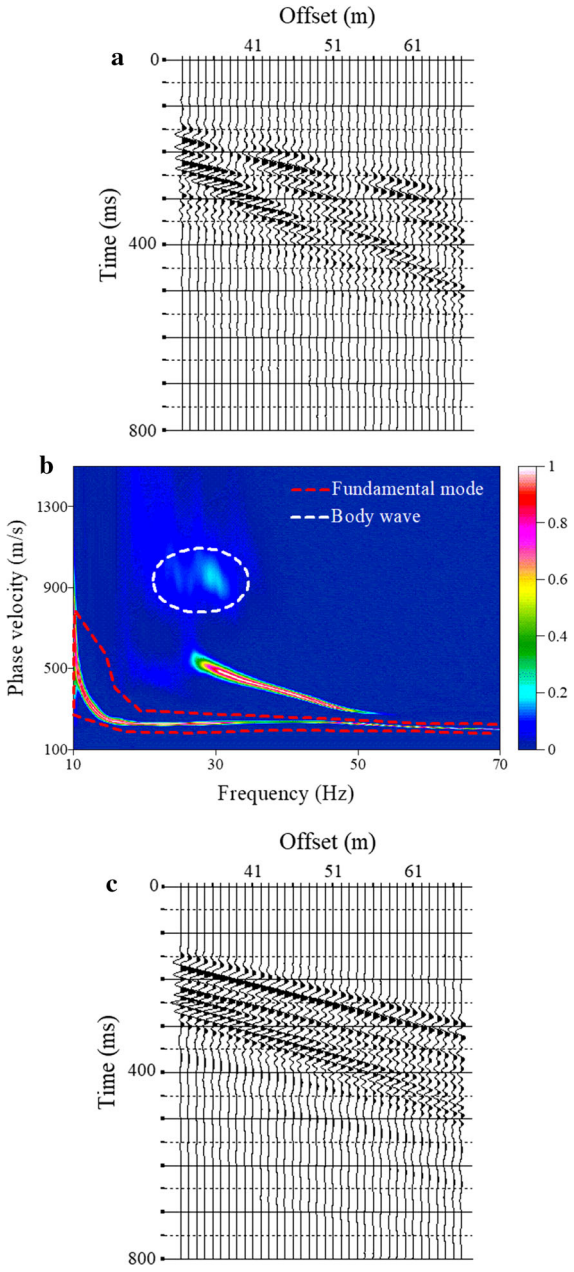

Figure 4
a Synthetic shot gather for the six-layer model. **b** Dispersion image of the shot gather obtained by high resolution linear Radon transform. The dark dots are theoretical phase velocities. The red contour line is the fundamental-mode energy range we selected. The white contour line is the body wave. **c** Fundamental-mode shot gather obtained from the dispersive energy selected in the red dashed contour line in (**b**)

Another six-layer synthetic model (Table 2) containing a low-velocity layer (Pan et al. 2013) is used to test the validity of our proposed method for calculating accurate attenuation coefficients. Rayleigh wave energy is clearly modeled in a 36-channel synthetic shot gather with 1 m interval (Fig. 4a). In the dispersion image obtained by a high-resolution LRT (Luo et al. 2008), a clear fundamental mode (red contour line, Fig. 4b) exists in the whole frequency band (10–70 Hz) and higher modes exist at a frequency range between 27 and 50 Hz. The body wave energy exists at a frequency range between 20 and 35 Hz with a higher velocity (white contour line, Fig. 4b).

The attenuation coefficients (blue line, Fig. 5) calculated directly from raw recording differ from their theoretical values (gray line, Fig. 5) calculated with Eq. (9) at the frequency ranges where body wave and higher modes exist. Fundamental mode is selected manually in the dispersion image (red contour line, Fig. 4b) and transformed into x–t domain to reconstruct the fundamental-mode shot gather (Fig. 4c). The attenuation coefficients (red line, Fig. 5) calculated from fundamental-mode shot gather give a satisfactory result compared to theoretical values, which proves the importance of performing mode separation in the data preprocessing.

In dissipative media, the relative frequency-dependent amplitude of recordings varies with offsets. The amplitude spectra of the raw data (Fig. 6a, b) decaying with the distance, however, are interfered by multi-modes and (or) body wave at some frequency range, in which the amplitude increase. The amplitude spectra (Fig. 6c, d) of the fundamental-mode shot gather do not suffer from the interference of the multi-modes and (or) body waves. The frequency-dependent amplitude decay with offset and have similar trend for increasing offset. The amplitude analysis present that the interference will cause inaccurate attenuation coefficients at some frequency ranges if the multi-modes and body wave are not excluded. Both synthetic examples present that mode separation helps us remove not only the influence of multi-mode surface wave, but also the possible influences of body waves, and prove the importance of performing amplitude-preserved mode separation prior to the estimating accurate attenuation coefficients.

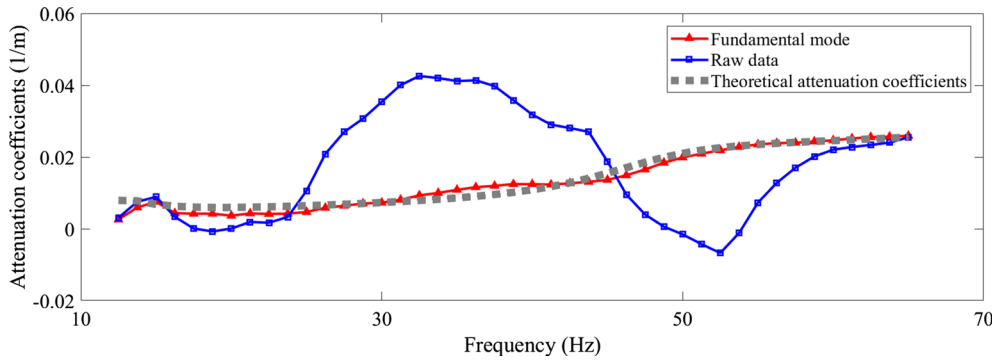

Figure 5
Comparison of attenuation coefficients obtained by different modes and theoretical attenuation coefficients

5. *Field Data*

A Love-wave field measurement was conducted at a mining site in Wyoming (USA) during the fall of 1998 to determine S-wave velocities of the near-surface materials (Xia et al. 2012, 2013). The test site is consisted of unconsolidated materials, which possibly has relatively low Q factors. Love-wave recordings were acquired using forty-eight 28 Hz horizontal-component geophones oriented in N–S direction. Geophones were deployed with an interval of 0.9 m along a W–E-oriented spread. A polarized seismic pulse was generated by a 6.3-kg hammer impacting a coupled plate, which was perpendicular to the spread. Two Love-wave seismograms (Fig. 7a, b) were recorded for two opposite source directions, one was a blow from the south and the other was from north. P-wave energy was eliminated, and Love-wave energy was strengthened by subtracting these two shot gathers. We only used the last 36 traces of the shot gather because dispersive Love waves were not fully developed in the short offsets (Fig. 7c). The spectra (Fig. 7d) indicated a strong energy loss and an interference may cause by higher modes and (or) body waves. Sharp dispersion image (Fig. 8a) was obtained by high resolution LRT. Higher mode appeared at the high-frequency range (> 30 Hz). We selected the fundamental-mode energy (green line, Fig. 8a) and then transformed it into t–x domain to get a single fundamental-mode shot gather (Fig. 8b). The corresponding spectra (Fig. 8c) showed a similar energy dissipation trend at the frequency range of 10–50 Hz compared with that in Fig. 7d. Attenuation coefficients (Fig. 9) obtained from the raw data and the fundamental-mode shot gather present a similar trend below 30 Hz, and become different at the high-frequency range (> 30 Hz) where the higher mode arises.

Fundamental-mode Love-wave phase velocities were picked along the continuous and sharp dispersive energy trend from 10 to 50 Hz, together with first higher mode appeared between 35 and 50 Hz (dark dots, Fig. 8a). We did a joint inversion of multi-modes dispersion curves to improve the accuracy of the estimated S-wave velocity. The phase velocities (red lines, Fig. 10a) calculated with the inverted S-wave profile fit with measured phase velocities well (blue lines, Fig. 10a), indicating the success of data fitting in the inversion. The inverted S-wave velocity (Fig. 10b) is comparable with the suspension Logging result, indicating relative high reliability of the inversion result.

Once the S-wave velocities were estimated, Q factors can be determined by inverting attenuation coefficients. We used the L-curve (Eq. 13) to determine an optimal regularization parameter and obtain a trade-off solution from a set of feasible solutions. A trade-off model with the damping factor (0.041) was indicated by a red square (Fig. 11a), which produced a model with a model length of 103.1 and data misfit of 0.00232. Attenuation coefficients (in blue circles, Fig. 11b) calculated based on the inverted Q factor model (Fig. 11c) fit attenuation coefficients calculated by Eq. (5) (in red square, Fig. 11b) reasonably

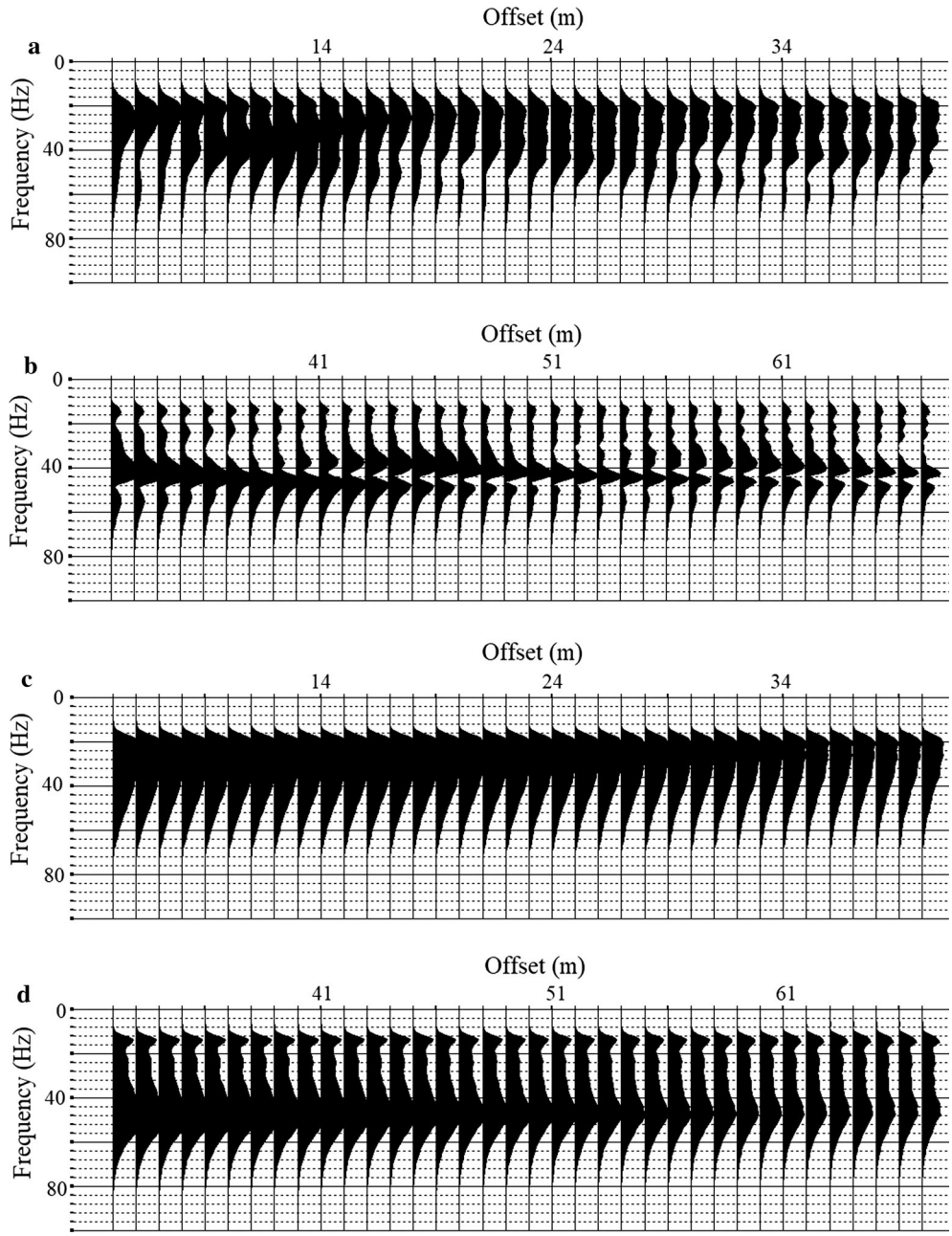

Figure 6
Amplitude spectra of raw shot gather and fundamental-mode shot gather. **a** and **b** are the amplitude spectra of raw shot gather in Figs. 2a and 4a, respectively; **c** and **d** are the amplitude spectra of fundamental-mode shot gather in Figs. 2c and 4c, respectively

well. The inverted Q factor profile showed two distinct interfaces: one was at a depth of 3 m and the other was at a depth of 12 m. According to the suspension Logging profile, materials in the top 2 m are soil and clayey sands (Fig. 10b), which are the unconsolidated sediments and usually have relatively low Q factor. In the middle part (2–12 m), the sediments are mainly composed by sands, sandstones, mudstones, which have relatively higher Q factor than that of soil. The deep parts (> 12 m) are mainly

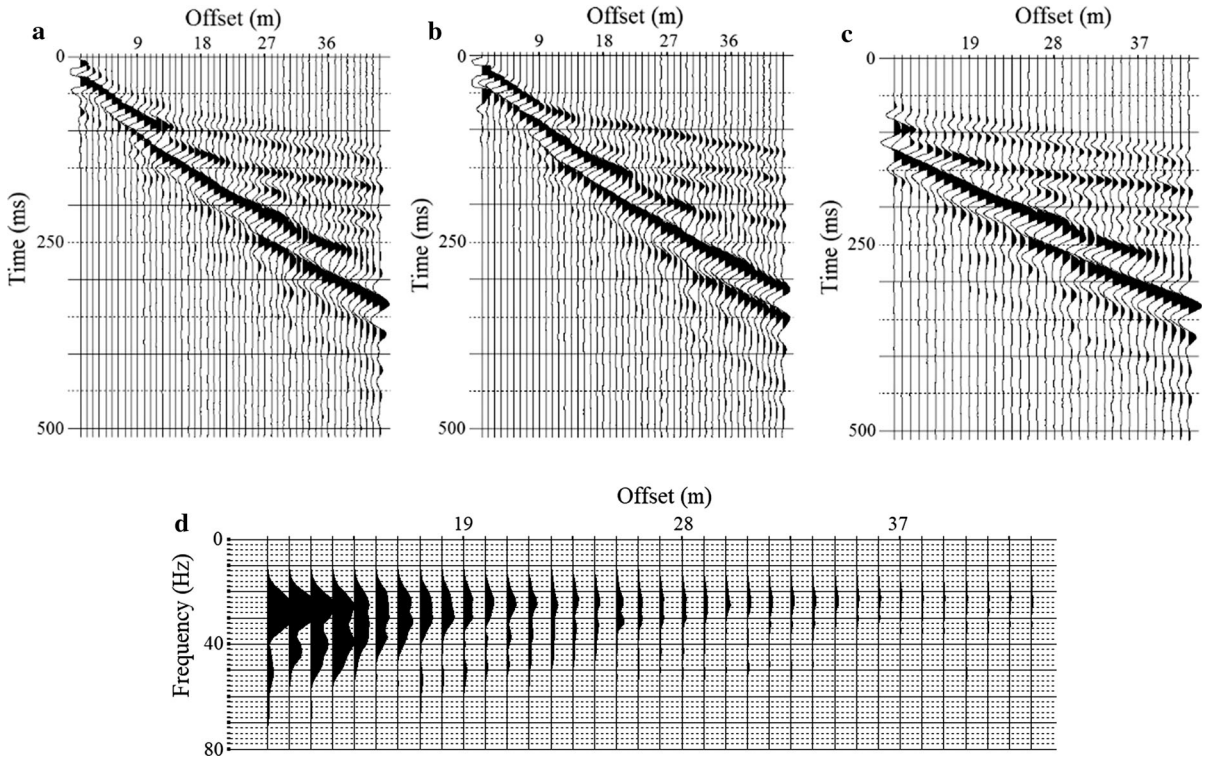

Figure 7
a and **b** Forty-eight-channel SH-wave refraction data along a W–E line. N–S blows against both ends of the fixture generated data with the polarity reversion of the first arrivals (**a** and **b**). **c** Last thirty-six traces of Love waves obtained by subtracting (**a**) and (**b**). **d** The amplitude spectra of raw shot gather (Fig. 7c)

consisted of coal, where Q factor gets lower than the middle part, despite of a similar S-wave velocity. The inverted Q factor is fairly reliable, which demonstrates the validity of our proposed method.

6. Discussion

Leaky wave may appear and contaminate Rayleigh wave shot gathers in shallow seismic. In the dispersion image, the dispersive energy of fundamental mode and leaky-wave mode is hard to be distinguished (Gao et al. 2014). The existence of leaky-wave mode influences not only the dispersion curve, but also attenuation coefficients acquired from shot gather. Attenuation coefficient obtained by Love-wave data is easier and more reliable comparing to Rayleigh waves because Love wave is independent with P-wave, and much less likely to be influenced by the existence of leaky surface wave. Thus, the utilizing of Love waves provides a more promising way in estimating near-surface S-wave velocity and Q factor comparing to Rayleigh waves.

In the previous work of Xia et al. (2013) about the estimation of Q factor from Love wave, they failed to find an "L" curve for choosing a proper damping factor and finally chose a damping factor of 0.1 by systematically trying all possible values. This might be caused by the neglecting of the influence of higher modes and body waves in the calculation of attenuation coefficients. It also leads to an underestimation of attenuation coefficients and an overestimation of Q factor in the inversion result. In this paper, we use the same data and perform a mode separation in the preprocessing to determine the correct attenuation coefficients. A proper damping factor can be determined from a clear "L curve" between data misfit and model length, which partly proves that the attenuation coefficients calculated after mode separation are more convincible.

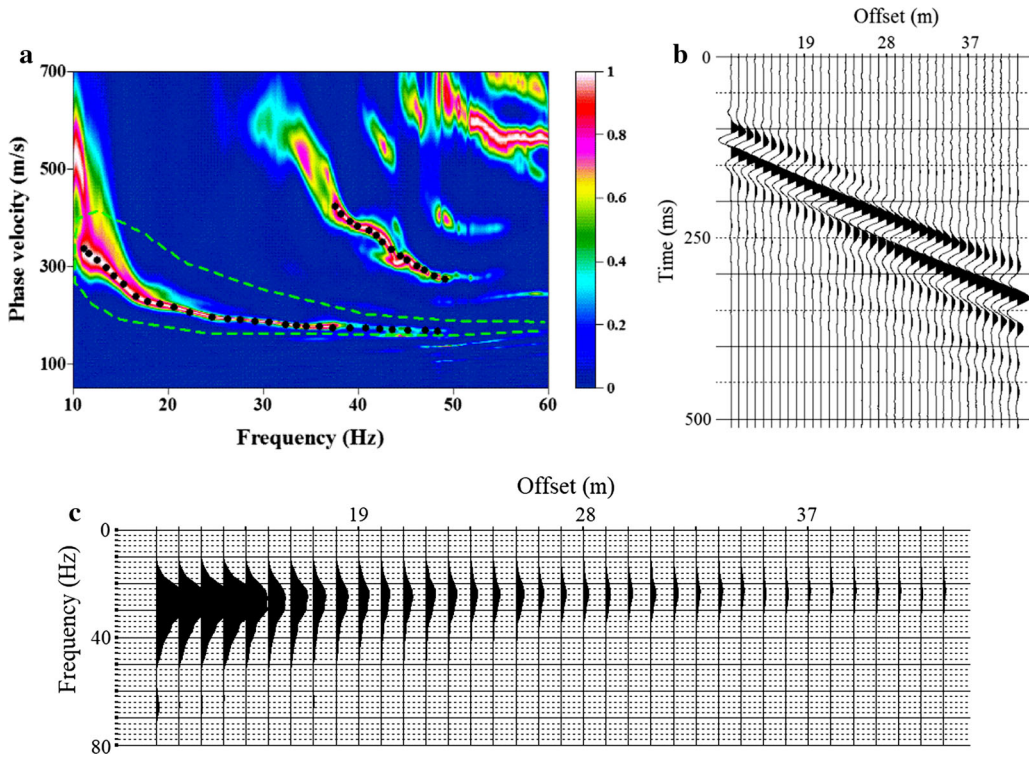

Figure 8

a Dispersion image of Love wave shot gather obtained by high-resolution linear Radon transform. The dark dots are the phase velocities picked for inversion. The green contour line is the fundamental-mode energy range we selected to reconstruct the fundamental-mode shot gather. **b** The fundamental-mode shot gather which is transformed from the dispersion energy selected by the green dashed line in (**a**). **c** Amplitude spectra of the fundamental-mode shot gather (Fig. 8b)

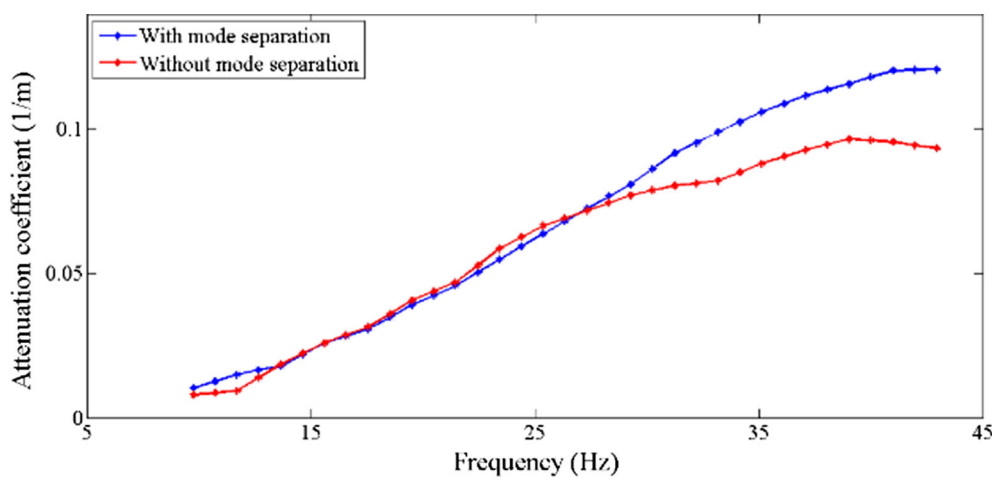

Figure 9

Comparison between the attenuation coefficients determined by the raw shot gather (Fig. 3c) and processed fundamental-mode shot gather (Fig. 4b)

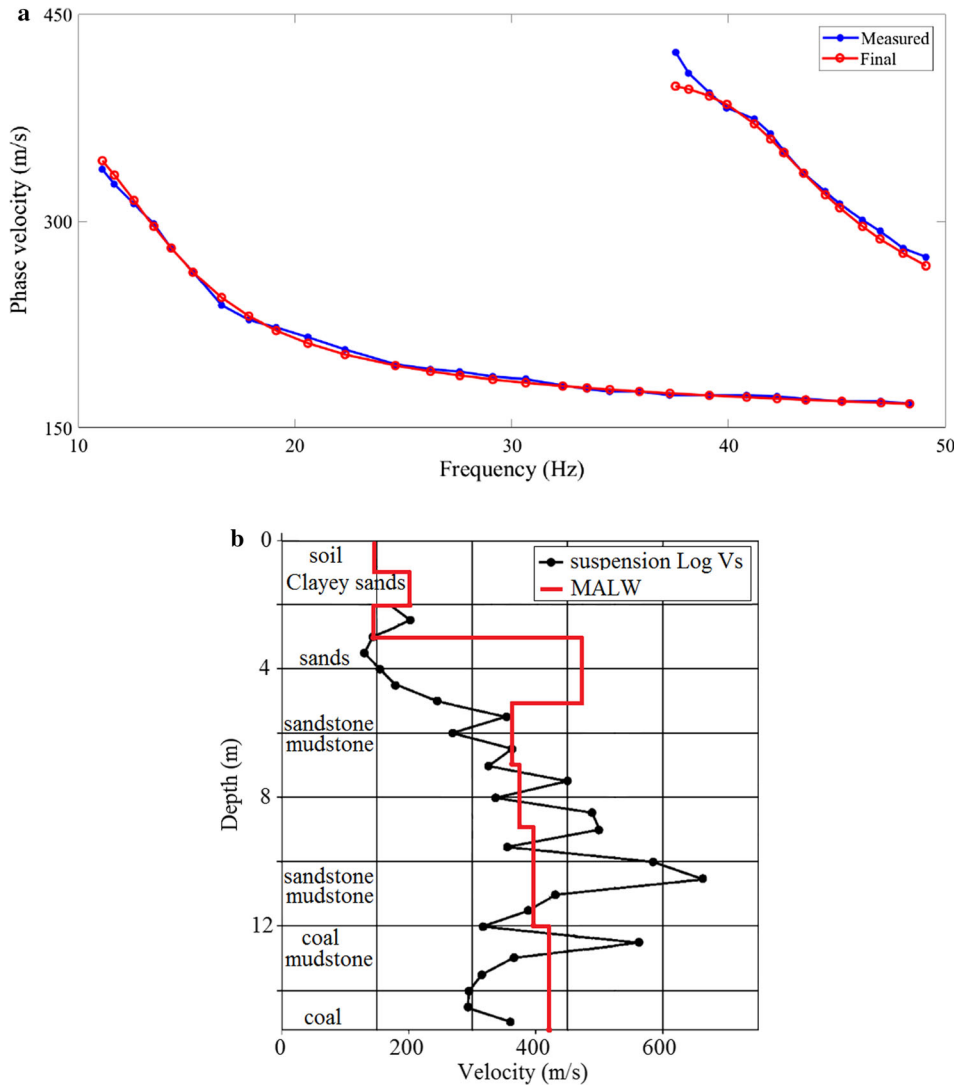

Figure 10

a Comparison between the picked phase velocities (labeled "Measured") and forward phase velocities calculated based on the inverted S-wave profile (labeled "Final"). **b** The comparison between inverted S-wave velocities and the suspension Log Vs results

7. *Conclusions*

We proposed to estimate near-surface Q factor by inverting attenuation coefficients with a linear damped inversion system. Two synthetic cases indicated that the presence of multi-mode surface waves and body waves will introduce errors in the attenuation coefficients if they are not excluded from the shot gather. Thus, an efficient mode separating as a pre-processing step is necessary for shallow-seismic recordings to determine correct attenuation coefficients. A real-world example demonstrated the necessity of mode separation in the pre-processing. The likelihood of the estimated Q factors is proved by the suspension Logging results, which proves the validity of our method. However, the accuracy of inverted quality factors that remains unchecked. A joint inversion of multi-mode surface-wave

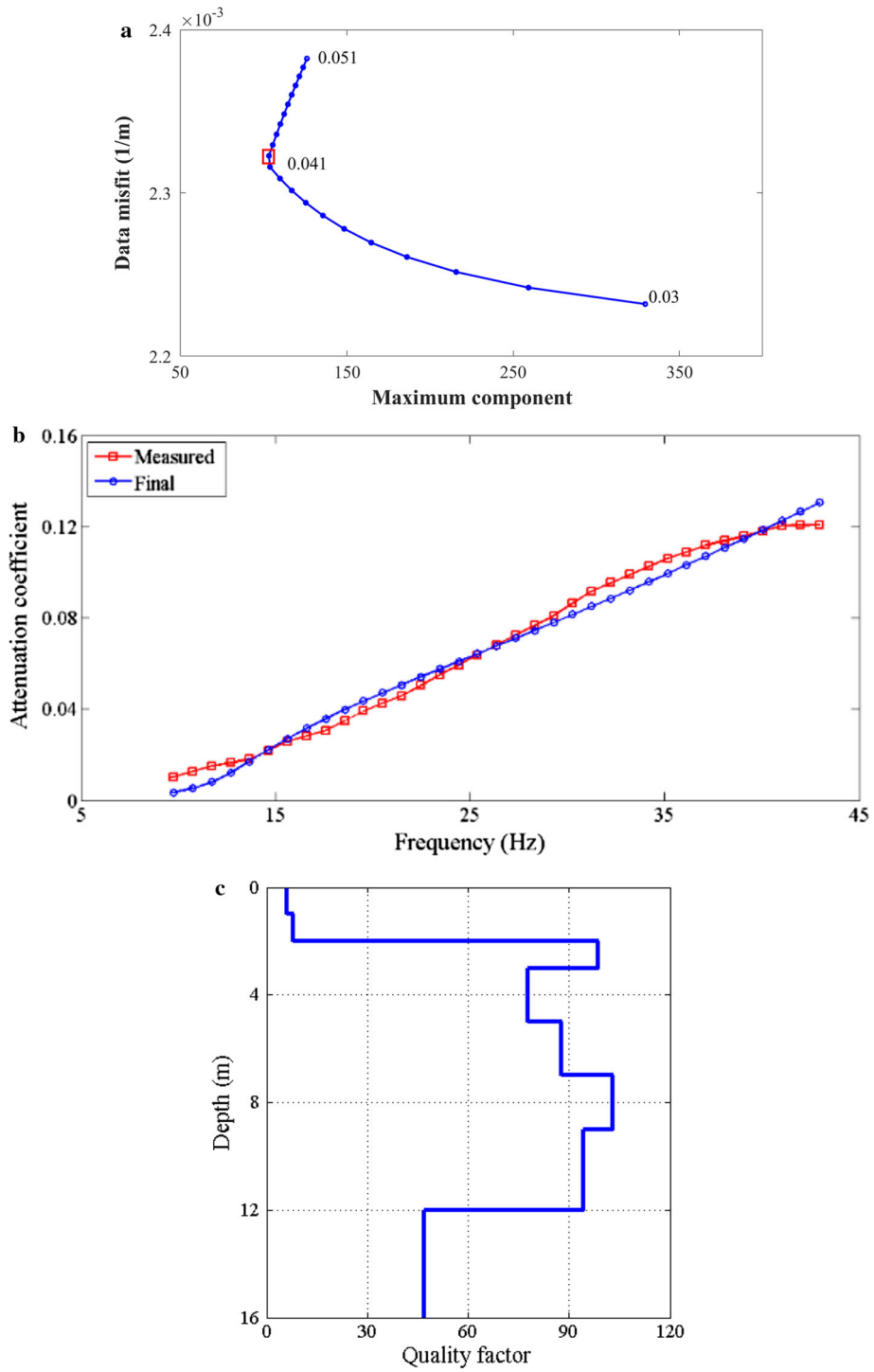

Figure 11

a The plot of "L" curve. **b** Comparison between the measured attenuation coefficients (labeled "Measured") calculated by Eq. (5) and forward attenuation coefficients (labeled "Final") calculated based on the inverted quality factor model. **c** Inverted Q factor profile

attenuation coefficients may increase the accuracy of inversion result, which deserves to be studied in the future.

Acknowledgements

We thank the Editor Ruben Tatevossian and two anonymous reviewers for their constructive and detailed comments. The authors also thank Bart Hoekstra of Blackhawk Geometrics for acquiring seismic data, and Thomas Bohlen for fruitful discussion. The author Lingli Gao would like to appreciate the funding provided by the National Postdoctoral Program for Innovative Talents under Grant No. BX201600131.

References

Aki, K., & Richards, P. G. (1980). *Quantitative seismology*. New York: W. H. Freeman and Company.

Anderson, D. L., Ben-Menahem, A., & Archambeau, C. B. (1965). Attenuation of seismic energy in upper mantle. *Journal of Geophysical Research, 70*(6), 1441–1448.

Bohlen, T. (2002). Parallel 3-D viscoelastic finite difference seismic modelling. *Computer and Geosciences, 28,* 887–899.

Foti, S., Parolai, S., Albarello, D., & Picozzi, M. (2011). Application of surface-wave methods for seismic site characterization. *Surveys In Geophysics, 32,* 777–825.

Gao, L., Xia, J., & Pan, Y. (2014). Misidentification caused by leaky surface wave in high-frequency surface wave method. *Geophysical Journal International, 199,* 1452–1462.

Gao, L., Xia, J., Pan, Y., & Xu, Y. (2016). Reason and condition for mode kissing in MASW method. *Pure and Applied Geophysics, 173,* 1627–1638.

Hansen, P. C. (1992). Analysis of discrete ill-posed problems by means of the L-curve. *Society of Industrial and Applied Mathematics Review, 34,* 561–580.

Hansen, P. C. (1998). *Rank-deficient and discrete ill-posed problems, numerical aspects of linear inversion*. Philadelphia: Society of Industrial and Applied Mathematics.

Ivanov, J., Tsoflias, G., Miller, R. D., & Peterie, S. L. (2014). *Near-surface Q_S and Q_P estimation from Rayleigh wave using multichannel analysis of surface waves (MASW) at an Arctic ice-sheet site*. Denver: SEG Annual Meeting.

Lawson, C. L., & Hanson, R. J. (1974). *Solving least-squares problems*. New Jersey: Prentice-Hall Inc.

Liu, H. P., Anderson, D. L., & Kanamory, H. (1976). Velocity dispersion due to anelasticity; implications for seismology and mantle composition. *Geophysics Journal International, 47*(1), 41–58.

Luo, Y., Xia, J., Miller, R. D., Xu, Y., Liu, J., & Liu, Q. (2008). Rayleigh-wave dispersive energy imaging by high-resolution linear Radon transform. *Pure and Applied Geophysics, 165*(5), 903–922.

Luo, Y., Xia, J., Miller, R. D., Xu, Y., Liu, J., & Liu, Q. (2009a). Rayleigh-wave mode separation by high-resolution linear Radon transform. *Geophysics Journal Internal, 179*(1), 254–264.

Luo, Y., Xia, J., Xu, Y., Zeng, C., Miller, R. D., & Liu, Q. (2009b). Dipping Interface mapping using mode-separated Rayleigh waves. *Pure and Applied Geophysics, 166,* 353–374.

Maraschini, M., & Foti, S. (2010). A Monte Carlo multimodal inversion of surface waves. *Geophysical Journal International, 182*(3), 1557–1566.

Misbah, A. S., & Strobbia, C. L. (2014). Joint estimation of modal attenuation and velocity from multichannel surface wave data. *Geophysics, 79,* 25–38.

Pan, Y., Xia, J., Gao, L., & Shen, C. (2013). Calculation of Rayleigh-wave phase velocities due to models with high-velocity surface layer. *Journal of Applied Geophysics, 96,* 1–6.

Shen, C., Xu, Y., Pan, Y., Wang, O., & Gao, L. (2016). Sensitivities of phase-velocity dispersion curves of surface waves due to high-velocity-layer and low-velocity-layer models. *Journal of Applied Geophysics, 135,* 367–374.

Socco, L. V., Foti, S., & Boiero, D. (2010). Surface wave analysis of building near surface velocity models established approaches and new perspectives. *Geophysics, 75,* A83–A102.

Werning, M., Boiero, D., Vermeer, P. (2013). Q estimation from surface wave. In *75th EAGE Conference & Exhibition incorporating SPE EUROPE 2013,* London, UK.

Xia, J., Miller, R. D., & Park, C. B. (1999). Estimation of near-surface shear-wave velocity by inversion of Rayleigh wave. *Geophysics, 64*(3), 691–700.

Xia, J., Miller, R. D., Park, C. B., & Tian, G. (2003). Inversion of high frequency surface waves with fundamental and higher modes. *Journal of Applied Geophysics, 52*(1), 45–57.

Xia, J., Miller, R. D., & Tian, G. (2002). Determining Q of near-surface materials from Rayleigh wave. *Journal of Applied Geophysics, 51,* 121–129.

Xia, J., Xu, Y., Luo, Y., Miller, R. D., Cakir, R., & Zeng, C. (2012). Advantages of using multichannel analysis of Love wave to estimate near-surface shear-wave velocity. *Surveys in Geophysics, 33,* 841–860.

Xia, J., Yin, X., & Xu, Y. (2013). Feasibility of determining Q of near-surface materials from Love waves. *Journal of Applied Geophysics, 95,* 47–52.

(Received November 6, 2017, revised March 5, 2018, accepted March 7, 2018, Published online March 16, 2018)